Supporting Information for "Wintertime Brine Discharge at the Surface of a Cold Polar Glacier and the Unexpected Absence of Associated Seismicity"

C. G. Carr[1,2], J. D. Carmichael[2], E. C. Pettit[3]

[1]University of Alaska Fairbanks, Fairbanks, AK, USA

[2]Los Alamos National Laboratory, Los Alamos, NM, USA

[3]Oregon State University, Corvallis, OR, USA

Contents of this file

1. Text S1 to S6
2. Figures S1 to S19
3. Table S1

Additional Supporting Information (Files uploaded separately)

1. Captions for Movies S1 to S2

Introduction

This supporting information includes: descriptions of the time-lapse photo timestamp correction (Text S1), details of the Rayleigh wave detection method (Text S2), dominant frequency and event duration analysis (Text S3), minimum pulse and phase sensitivity

---

Corresponding author: Chris G. Carr, Los Alamos National Laboratory, Los Alamos, NM 87544, USA (cgcarr@lanl.gov)

analysis (Text S4), source depth analysis (Text S5), and context for the 19 additional figures, 1 table, and 2 movies (description and context in Text S6).

Text S1. Time-lapse Photo Timestamp Correction

Upon review of data collected by the time-lapse camera, we realized that the time zone corresponding to the internal camera clock had not been recorded. Field photos taken on personal cameras during the time-lapse camera installation as well as metadata from a co-located seismometer guided our time zone correction of the time-lapse images from the camera. The camera time appears to correspond to UTC-13 at the time of installation, and the camera clock observes daylight savings time following the dates for the United States. We therefore add 12 hours for timestamps between 9 March and 2 November 2014, and add 13 hours during the rest of the year. We estimate that our corrected times of day are within about 1–2 hours of the true time of day based on sunlight patterns. Despite the lack of temporal accuracy, we can still make observations about the relative timing of brine release pulses as well as erosional and depositional characteristics; however, we cannot tie any specific photo to discrete seismic events. We note that even with accurate timestamps, the relatively coarse time resolution of the photos (1 sample every 2 hours) would hinder direct correlation with specific events in the seismic record (200 samples per second).

Text S2. Rayleigh Wave Detection Method

Rayleigh waves are seismic waves characterized by out-of-phase displacement in the vertical and radial plane that connects the seismic source to the sensor; displacement

decays exponentially with depth from the surface. Particle motion plots of the vertical component of surface motion against the horizontal component show retrograde (counter-clockwise), elliptical motion in the direction of wave propagation, as a function of time (Stein & Wysession, 2003, p. 87–89). These characteristics can be used to construct a correlation detector to identify Rayleigh waves in a seismic data stream.

We follow similar starting principles as Chael (1997) to construct our Rayleigh wave detector. Namely, we phase-advance the vertical channel by $\pi/2$ and correlate the result with a horizontal channel to look for high correlation values. In contrast to Chael (1997), we do not rotate the horizontal channel through a range of potential back azimuths – instead we assume a back azimuth consistent with a Blood Falls source and monitor for activity.

We exploit both tails of the correlation density function to monitor for Rayleigh waves traveling in opposite directions. A high absolute value of correlation between a horizontal channel and a Hilbert-transformed vertical channel indicates elliptically polarized particle motion in the plane defined by the horizontal and vertical channels. The sign of the correlation indicates the direction of wave travel. In a Blood Falls-centric reference frame: large positive values indicate waves traveling towards the seismometer from the Blood Falls direction, and large negative values indicate waves traveling away from the seismometer towards Blood Falls.

In order to detect statistically significant, retrograde elliptical particle motion indicative of Rayleigh waves, and save out the relevant data and event detection statistics, we performed the following operations.

1. We pre-processed the three-channel data for each station; we

(i) Detrended the data to remove the best straight-line fit from the data,

(ii) Filtered over 2.5–35 Hz with a bandpass, 4th order minimum phase Butterworth filter, and

(iii) Removed any samples for which data was not recorded on all three channels to equalize vector data length (required for subsequent matrix operations).

2. We rotated the seismogram data into a Blood Falls-centric horizontal reference system. Because we are interested in seismic sources near Blood Falls, we prescribed back azimuths to rotate the North (N) and East (E) channels into a radial (R) and transverse (T) orientation relative to Blood Falls using the equation:

$$\begin{bmatrix} R \\ T \end{bmatrix} = \begin{bmatrix} \cos\theta & \sin\theta \\ -\sin\theta & \cos\theta \end{bmatrix} \begin{bmatrix} N \\ E \end{bmatrix}, \tag{1}$$

where θ is the heading pointing from the seismometer towards Blood Falls, measured clockwise from the north (Incorporated Research Institutions for Seismology (IRIS), 2020). Rotation angle values used for θ are CECE: 330°, KRIS: 140°, and JESS: 70°. We performed a 2D rotation, since the seismometers are close together and we are interested in shallow, local sources.

3. We Hilbert transformed the vertical channel by performing a frequency independent phase advance of $\pi/2$.

4. We calculated cross-correlation between the aligned channel pair of the Hilbert-transformed vertical and radial channels, hereafter 'ZR'. The correlation process implemented a 0.75 second, tapered, sliding mid-point centered window.

5. We ran the correlation detector on both of the resulting ZR correlograms as follows:

(i) Correlograms were subset into 30-minute windows. For each 30-minute window, we: calculated the normalized data histogram based on the correlogram (e.g., the histogram in Figure 2b is calculated from the correlogram in Figure 2c), implemented MATLAB `normfit.m` to estimate the normal distribution parameters $\hat{\mu}$ (sample mean) and $\hat{\sigma}$ (sample standard deviation) of the middle 95% of the normalized data histogram, and calculated the fit error between this histogram and the theoretical PDF. The large-sample normality assumption for the correlation statistic is justified elsewhere (Wiechecki-Vergara et al., 2001).

(ii) Using the parameter estimates from the previous step, we calculated the probability density function (PDF) of the standard normal distribution evaluated at the same bin locations as the full data histogram.

(iii) We inverted the PDF to find the threshold corresponding to the desired CFAR and identified samples of the correlogram that exceed the detector threshold. In detail, we ran the detector with one-sided CFAR thresholds of $5\text{x}10^{-5}$ and $5\text{x}10^{-6}$. We calculated the threshold for both tails of the distribution separately for a given one-sided CFAR.

6. From the subset of threshold-exceeding correlation values identified in the previous step, we defined events. An event declaration required a minimum temporal separation from preceding or succeeding events (3.29 seconds). High correlation values with less temporal separation were grouped together. An event declaration also required at least 0.31 seconds duration between the first and final threshold exceedance ("trigger on" and "trigger off" times described in Figure 2d caption).

7. The highest correlation value and associated timestamp within the resulting block were saved as the event detection and time. We also calculated the p-value of the event detection statistic.

8. We ran the detector for each station for both tails in the ZR and ZT correlation distributions (corresponding to four source back azimuths per station) and for each of the two, one-sided CFAR thresholds. In this paper, we present the results corresponding to the right-tail of the ZR correlation distribution, 'ZR+', where events indicate waveforms traveling from the direction of Blood Falls toward the receiver. For simplicity, we refer to 'ZR+' as 'ZR' throughout this paper because we do not discuss the ZR- events.

We selected a minimum event duration of 0.31s based on visual inspection of waveforms detected under different duration requirements.

Text S3. Dominant Frequencies and Event Durations of Detected Rayleigh Events

To further investigate temporal variation in event duration and frequency throughout the year, we conduct the following analysis using the event catalogs generated by running the Rayleigh event detector. Each event catalog is defined as the collection of events identified from one station using a specific CFAR condition and back azimuth (ZR$\pm$ or ZT$\pm$, as defined by the preset rotation values, see Supporting Information Text S2). For instance: events identified at CECE with a back azimuth pointing towards the Blood Falls source region (ZR in Figure 2a) under a CFAR condition of $5\text{x}10^{-6}$ compose a catalog.

For each event identified by the detector under a specified CFAR condition, the duration of the event is defined as the total time elapsed between the first and final threshold

exceedance within the event declaration (Figure 2d). Therefore, even if the same event is identified under multiple CFAR conditions, the event will have different event durations under different threshold conditions, and shorter durations will correspond to larger threshold values (lower CFAR values).

The dominant frequency within the passband ([2.5,35] Hz) for each event was calculated as follows: event start and end times from the detector output were used to extract seismogram data from the original SAC files. These data were then detrended, filtered, and rotated using the same methods as implemented in the event detector. We calculated the dominant frequency following Douma and Snieder (2006, equation 3).

Our examination of event detection rates did not point to any clear changes leading up to or coinciding with the initial visible brine release period. We also examined event duration and dominant frequency time series, but these characteristics likewise showed no changes we could clearly link with brine release. However, we did note differences between stations and seasons in dominant frequencies of detected events. The following analysis describes the variability of baseline changes in dominant frequencies throughout the observation period.

We plot dominant event frequency (on the vertical channel) against time of day in Figure S6, binned by month of year. Because our seismic experiment spanned November 2013–January 2015, a few month bins include data for more than one year, depending on station data availability. Darker colors represent events identified under smaller CFAR conditions (larger threshold values). As expected, more events are identified under the larger CFAR value.

At all stations, the dominant frequencies of detected Rayleigh events spans the passband ([2.5, 35] Hz), but visually cluster around certain frequency bands. Prominent examples include the strong horizontal bands between 20–30 Hz for land-based station CECE during March through October (Figure S6a). Dominant frequency patterns vary throughout the day during the summer. In particular, at on-ice station JESS in November (and to some extent in December), more events are detected and across a wider frequency band from 18:00–06:00 UTC; while from 06:00-18:00 UTC, dominant frequencies group toward the upper range of the passband (Figure S6c). A similar, but muted, pattern is apparent at CECE in November and December.

Text S4. Minimum Pulse Width and Phase Sensitivity

We demonstrate the minimum pulse width we could observe from a source about 500 m away given our experimental design (including our filter band, Nyquist frequency, and instrument response). To do this, we construct an internally consistent model that constrains the temporal width of a Rayleigh wave that is sourced at Blood Falls and recorded at our receiver 500 m away, after it dispersively attenuates through our half-space, 'lossy' model. We use the Futterman filter to provide this attenuation and dispersion, which has a frequency domain representation (Carmichael et al., 2015) of

$$e^{-t^*|\omega|/2+j\omega t^*/\pi \ln(|\omega|/2\pi f)} \tag{2}$$

where ω is angular frequency, t^* is travel time normalized by quality factor Q, j is the imaginary unit, $\ln(x)$ is the natural logarithm of argument x, and f is a reference frequency that we take to be the Nyquist frequency (100 Hz) of our sensor; smaller reference frequencies lead to more lossy mediums. To form this pulse, we propagated a delta-

function signal from the source to the receiver with a Futterman filter (Futterman, 1962). We parameterized this filter with a quality factor of Q=40 (consistent with the attenuation value we use for the minimum detectable source size analysis in Section 3.3) and a Rayleigh wave speed of about 1.7 km/s. This is equivalent to the more common parameter representation that uses a t^* value (a key Futterman filter parameter) of $t^* = D/Qc_R$, where D is the distance between the source receiver and c_R is the Rayleigh wave speed. This operation dispersively attenuates the source pulse and thereby causally (or nearly so) broadens the pulse.

We then convolved this pulse with the L-22 geophone instrument response, which further broadens the pulse. In the absence of noise, such a pulse shows an apparent temporal width of about 0.4 s (blue arrows, Figure S9). The presence of noise would reduce this effective pulse width to be confined to the region that proceeds the large positive swing and includes the broader negative swing back to positive displacement (perhaps 0.2 s). We note that the units of counts on the vertical axis are arbitrary in the absence of noise.

However, we find that within that 0.4 s pulse duration that about 14 cycles fit at our highest frequency (35 Hz multiplied by 0.4 s; Figure S10), and about one full cycle fits at our lowest frequency (2.5 Hz multiplied by 0.4 s; Figure S11). Therefore, our Rayleigh wave detector will compare at waveforms with at least one full cycle because we require a minimum threshold exceedance of at least 0.31 s to declare an event.

Next, we consider the impact of phrase shift. As described above, we model the minimum duration pulse that propagates from a source located 500 m from a receiver. To do this, we propagate a delta function through our dispersively attenuating medium with a Futterman filter, and then convolve the instrument response of our L-22 receiver into this

resulting pulse. We then produce a frequency modulated waveform within the passband of our 2.5 to 35 Hz filter by multiplying the resulting pulse model by a 10 Hz sinusoid. Next, we phase advance one of two copies of this signal by a set of phases between 45 and 135 degrees. We perform this phase advance by using Equation 5 in Box 5.6 from Aki and Richards (2009, p. 153) to express the phase advanced function as the original vertical channel signal, multiplied by the cosine of the phase shift, plus the Hilbert transform of the vertical channel signal, multiplied by the sine of the phase shift. Lastly, we injected these signals into noise such that the signal to noise ratio of the resultant seismograms, over their signal duration (0.4 s) was 10 (equivalent to 20 dB; Figure S12). This operation visibly produced a phase shift between the radial and vertical channels (Figure S13). We then computed the sample correlation coefficient between the radial channel seismogram and the transformed vertical channel seismogram to quantify how errors in the phase-advance assumption degraded our peak correlation coefficient (Figures S14 and S15). We compared these correlation coefficient detection statistics, as output by our Rayleigh wave detector, against the constant false alarm rate threshold ($5\text{x}10^{-6}$); the correlation threshold was about 0.58 for these data. Our data show that the peak correlation coefficient remains above this threshold, even when the phase error is as absolutely large as 45°; this appears to inconsistently trigger our detector according to our trigger criteria. We also note that a positive phase error (so that the phase shift is +135°rather than -45°) leads to larger peak correlation coefficients. Therefore the errors are asymmetric, and negative errors relative to 90°could lead to more Rayleigh wave correlation detection losses when compared to positive errors.

Text S5. Source Depth Analysis

We perform the following analysis to estimate the maximum potential Rayleigh-wave generating source depths we sample with the frequencies used in our seismic experiment. Sources deeper than this estimate could evade detection, given our experimental design (including factors like receiver locations and frequencies used in our seismic experiment).

In doing so, we estimate the source size required to produce a waveform of a given amplitude at a receiver location. Our solution is approximate, and uses results from Chapter 7, Aki and Richards (2009). In particular, we generate half-space eigenfunctions, but use dispersive relationships present in a layer–over–half-space.

In our layer–over–half-space configuration, the top 50 m thick layer represents the cold ice of Taylor Glacier and the half-space represents the subglacial basement. Widespread, saline-saturated sediments are known to exist beneath Taylor Glacier; the thickness of this layer under the terminal kilometer of the glacier is on the order of at least tens of meters (Mikucki et al., 2015, Figure 3). We do not include this layer in our model. We further make the simplifying assumption that the glacier ice is homogeneous, in contrast to the more complicated reality of a stiff, relatively clean ice layer overlying a much more deformable, debris-rich basal ice layer (Pettit et al., 2014).

We use the same model input values as a prior seismic study at Taylor Glacier (Carmichael et al., 2012), which was informed by an active seismic survey conducted in nearby Beacon Valley (Shean et al., 2007). Specifically, we use p-wave and s-wave speeds of 3850 m/s and 1950 m/s for the ice layer and 4800 m/s and 2900 m/s for the substrate half-space. We use a standard ice density of 917 kg/m^3 and a substrate density

of 2700 kg/m^3 consistent with basement velocities in Taylor Valley (Table 1, Barrett & Froggatt, 1978, and references therein).

Following Aki and Richards (2009, p. 328), we solve for Rayleigh wave displacement using

$$\mathbf{u}^{\mathrm{RAYLEIGH}}(\mathbf{x},\omega) = \mathbf{G}^{\mathbf{R}}[U_1 + U_2\cos(2\phi) + U_3\sin(2\phi)], \tag{3}$$

where $\mathbf{u}^{\mathrm{RAYLEIGH}}$ is the displacement, dependent on the source-receiver distance ($\mathbf{x}$) and angular frequency (ω). $\mathbf{G}^{\mathbf{R}}$ is the azimuthally-independent displacement vector described below. Coefficients U_1, U_2, and U_3 describe the radiation pattern, with azimuthal angle ϕ between the source and receiver. We use the radiation pattern for a crack opening in the direction of the receiver to maximize the total displacement. We refer the reader to Carmichael (2021, equation 39) and Carr, Carmichael, Pettit, and Truffer (2020, Appendix C) for further documentation of the radiation pattern specific to the crack opening.

We solve for the eigenfunction $r_1(h)$ in the azimuthally-independent displacement vector (Aki & Richards, 2009, p. 328):

$$\mathbf{G}^{\mathbf{R}}(\mathbf{x};h,\omega) = \sum_n \frac{k_n r_1(h)}{8cUI_1}\ \sqrt{\frac{2}{\pi k_n r}}\ e^{\left[i\left(k_n r - \frac{\pi}{4}\right)\right]}\ [r_1(z)\hat{\mathbf{r}} + ir_2(z)\hat{\mathbf{z}}], \tag{4}$$

where $r_1(h)$ is horizontal displacement at the unknown source depth h. We use eigenfunctions $r_1(z)$ and $r_2(z)$ (vertical displacement) for the half-space below the surface layer for each term in the sum, and populate their exponential arguments with the wave number k_n from the dispersion relationship (previously calculated for the minimum detectable event size analysis, see Section 3.3 in the main text). Other terms in equation 4 include: phase velocity $c = \omega/k_n$ (angular frequency divided by wave number), group velocity U, and energy integral I_1 (for a full description, see Carmichael (2021) and Appendix C in

Carr et al. (2020)). Figure S17 shows the displacement for the r_1 and r_2 eigenvectors for frequencies of 2.5 and 35 Hz.

To relate the correlation coefficient output by the Rayleigh wave detector to the threshold source size, we use the relationships between signal-to-noise ratio (SNR), the sample correlation, and the target waveform amplitude. We first note that the SNR of a noisy signal is representable as the correlation coefficient ρ between waveforms of the same shape:

$$\mathrm{SNR} = \frac{\rho}{1-\rho}. \tag{5}$$

where ρ, in this case, is the value of the correlation threshold required for a meaningful detection (defined by a specific CFAR condition) and SNR is the square of the Rayleigh waveform amplitude, divided by the noise energy. The noise energy is the estimated sample variance $\hat{\sigma}^2$ multiplied by one less the number of samples $(N-1)$ in the Rayleigh wave detector window:

$$\mathrm{SNR} = \frac{||\mathbf{u}^{\mathrm{RAYLEIGH}}||^2}{\hat{\sigma}^2(N-1)}. \tag{6}$$

We substitute equation 6 into equation 5 to relate threshold Rayleigh wave size (numerator of equation 6) to the estimated noise variance and correlation threshold. We approximate $\mathbf{u}^{\mathrm{RAYLEIGH}}$ using the content on page 328 of Aki and Richards (2009) described above (equation 3), which then provides a relationship between $r_1(h)$ (a function of source depth) and the estimates from the data. The equality that outputs source depth therefore includes analytical formulation; numerical calculation of the dispersion relationships to compute phase velocity c, group velocity U, and the wavenumber versus frequency relationship (k_n); and both noise and deterministic parameter estimates from the data ($\hat{\sigma}^2$, ρ and N).

We selected the same three weeks (10-30 May 2014) used in the prior detector threshold analyses, calculated sample variance from the pre-processed (detrended, filtered, rotated) data, and extracted detector thresholds from the Rayleigh detector results under the $5x10^{-6}$ CFAR condition (Table S1).

We chose the values from Table S1 for each station that would provide the shallowest source for the detection limit, namely: the largest threshold and highest sample variance. For all stations, we find that sources depths shallower than about 2.5 km produce displacement above the detection limit. Specifically, for land-based stations CECE the threshold detection depth is 2.9 km, at KRIS the threshold detection depth is 2.6 km and for on-ice station JESS the threshold detection depth is 2.5 km. We conclude that our Rayleigh wave detector would trigger on elliptically polarized waveform data sourced by a crack emplaced at shallower depths than $\sim$2.5 km in the observed noise environment.

Text S6. Description of Additional Figures

A large crack in the glacier surface was visible following the winter 2014 brine release (Figure S1). This photo from 21 November 2014 shows the brine icing largely intact, with some incised meltwater channels. The lake ice and moat appear to be still frozen.

We generated spectrograms from the seismic data in order to perform a visual data quality check and to qualitatively investigate potential relationships between meteorological variables and spectral features. Spectrograms were generated from the detrended, bandpass-filtered ([2.5, 35] Hz) data using 8 second windows with 5 second overlap. For this initial analysis, we did not remove the instrument response; therefore, the units are related to amplitude in counts rather than ground displacement or velocity.

In Figures S2, S3, and S4, temperature (left y axis) and wind speed (right y axis) are plotted on the upper panel of each subplot; scales vary from month to month to accommodate seasonality. Meteorological data are from the Taylor Glacier station (Doran & Fountain, 2019). The three channels (EHZ: vertical, EHE: East, and EHN: North) are plotted in the lower three panels of each subplot.

We visually inspected spectrograms to identify time periods when data quality was poor, and excluded these days from the Rayleigh wave detection analysis. Examples include data from station CECE prior to servicing in January 2014 (Figure S2a) and station JESS after 9 December 2014 (Figure S4b). During the onset of brine release in May 2014 (Figure S3), we deemed data quality on all channels at all stations to be sufficient for the Rayleigh wave analysis. Examples of detected waveforms are included in Figure S5.

In Figures S6, S7, and S8 we plot dominant frequency of identified Rayleigh wave events arriving at each seismic station from a Blood Falls back azimuth against time of day (Figures S6) or the event duration (Figures S7 and S8). Dominant frequency and event duration are calculated as described in the Text S3 above. In Figure S7, each station's subplot includes all data for all identified Rayleigh events, while in Figure S8 the events are separated by month of year. Event duration clusters strongly around 0.6–0.7 seconds, and the distribution of event times is skewed to the left (shorter event duration) with a long right-hand (longer event duration) tail. The clustering of event times suggests a repetitive source with a given physical dimension.

Figures S9–S15 are described in Text S4 above.

Our Rayleigh detector exploited both tails of the statistical distribution as well as correlation between the vertical and transverse channels (with respect to a Blood Falls

back azimuth) to detect Rayleigh events arriving from other directions. We plot results from one back azimuth, the ZR back azimuth, representing Rayleigh waves traveling from Blood Falls to the sensor in Figure S16 (see Figure 2 for back azimuth directions). The lighter shade of blue on each time series are the event detection rates for a CFAR of $5x10^{-5}$; the bold lines are the detection rates with a CFAR of $5x10^{-6}$. The initial Blood Falls brine release is highlighted in red for the CFAR = $5x10^{-6}$ results on all plots.

A meteorological station (Doran & Fountain, 2019) located on Taylor Glacier collected air temperature and wind speed during the duration of our seismic experiment (Figure S16g). A previous study at Taylor Glacier modeled melt occurring at temperatures as low as -2.7°C during the summer season due to solar radiation (Hoffman et al., 2008). However, the brine release events documented in our study occurred when air temperatures were well below this threshold; therefore, we assume negligible surface melt. Air temperatures at the Lake Bonney meteorological station (located on dark rocks and sediment on the south shore of Lake Bonney) follow a similar pattern and are slightly warmer yet still subfreezing. Warm air temperature spikes during winter months correspond with increases in wind speed (Nylen et al., 2004; Speirs et al., 2010).

In Figure S17, the normalized vertical and horizontal displacement for the Rayleigh eigenfunctions associated with our source model from Text S5 above are plotted as a function of depth. As described in Text S5, we used the detector threshold values and sample variance from Table S1 as input values to constrain our source depth model.

Various cracks in ice are present in the environment near the glacier terminus (Figure S18), including ice blisters (Figure S19). The approximate scale of these cracks ranges from tens of centimeters to several meters in length, with openings on the order of cen-

timeters to tens of centimeters.

Movie S1. Movie created from time-lapse photos, one image per day from 9 May 2014 – 7 June 2014. See Text S1 above for an explanation of the time zone correction we applied; all time stamps are given in our best estimate of UTC time. File name: ms01.mp4.

Movie S2. Movie created from time-lapse photos, one image per 2 hours except when power loss interrupted data collection. Note the movie retains a placeholder of the most recently available image while the counter in the lower left advances, these frames are labeled like "no data, image from 08-Jun-2014 16:47 UTC". See Text S1 above for an explanation of the time zone correction we applied; all time stamps are given in our best estimate of UTC time. File name: ms02.mp4.

References

Aki, K., & Richards, P. G. (2009). *Quantitative Seismology* (Second ed.). Mill Valley, CA, USA: University Science Books.

Barrett, P. J., & Froggatt, P. C. (1978). Densities, porosities, and seismic velocities of some rocks from Victoria Land, Antarctica. *New Zealand Journal of Geology and Geophysics*, *21*(2), 175–187. doi: 10.1080/00288306.1978.10424049

Carmichael, J. D. (2021). Hypothesis tests on Rayleigh wave radiation pattern shapes: a theoretical assessment of idealized source screening. *Geophysical Journal International*, *225*(3), 1653–1671. doi: 10.1093/gji/ggab055

Carmichael, J. D., Joughin, I., Behn, M. D., Das, S., King, M. A., Stevens, L., & Lizarralde, D. (2015). Seismicity on the western Greenland Ice Sheet: Surface

fracture in the vicinity of active moulins. *Journal of Geophysical Research F: Earth Surface*, *120*(6), 1082–1106. doi: 10.1002/2014JF003398

Carmichael, J. D., Pettit, E. C., Hoffman, M., Fountain, A., & Hallet, B. (2012). Seismic multiplet response triggered by melt at Blood Falls, Taylor Glacier, Antarctica. *Journal of Geophysical Research: Earth Surface*, *117*(F3), 16 pp. doi: 10.1029/2011JF002221

Carr, C. G., Carmichael, J. D., Pettit, E. C., & Truffer, M. (2020). The influence of environmental microseismicity on detection and interpretation of small-magnitude events in a polar glacier setting. *Journal of Glaciology*, *66*(259), 790–806. doi: 10.1017/jog.2020.48

Chael, E. P. (1997). An automated Rayleigh-wave detection algorithm. *Bulletin of the Seismological Society of America*, *87*(1), 157–163.

Doran, P. T., & Fountain, A. G. (2019). *McMurdo Dry Valleys LTER: High frequency measurements from Taylor Glacier Meteorological Station (TARM) in Taylor Valley, Antarctica from 1994 to present.* Environmental Data Initiative. doi: 10.6073/pasta/a1df5cdab3319e9adeb18f8448fd363e

Douma, H., & Snieder, R. (2006). Correcting for bias due to noise in coda wave interferometry. *Geophysical Journal International*, *164*(1), 99–108. doi: 10.1111/j.1365-246X.2005.02807.x

Futterman, W. I. (1962). Dispersive body waves. *Journal of Geophysical Research*, *67*(13), 5279-5291. doi: 10.1029/JZ067i013p05279

Hoffman, M. J., Fountain, A. G., & Liston, G. E. (2008). Surface energy balance and melt thresholds over 11 years at Taylor Glacier, Antarctica. *Journal of Geophysical*

Research, *113*(F4), 12 pp. doi: 10.1029/2008JF001029

Incorporated Research Institutions for Seismology (IRIS). (2020). *IRIS DMC IRISWS rotation Web Service Documentation.* http://service.iris.edu/irisws/rotation/1/.

Mikucki, J. A., Auken, E., Tulaczyk, S., Virginia, R. A., Schamper, C., Sørensen, K. I., ... Foley, N. (2015). Deep groundwater and potential subsurface habitats beneath an Antarctic dry valley. *Nature Communications*, *6*(6831), 9 pp. doi: 10.1038/ncomms7831

Nylen, T. H., Fountain, A. G., & Doran, P. T. (2004). Climatology of katabatic winds in the McMurdo Dry Valleys, southern Victoria Land, Antarctica. *Journal of Geophysical Research*, *109*(D03114), 9 pp. doi: 10.1029/2003JD003937

Pettit, E. C., Whorton, E. N., Waddington, E. D., & Sletten, R. S. (2014). Influence of debris-rich basal ice on flow of a polar glacier. *Journal of Glaciology*, *60*(223), 989–1006. doi: 10.3189/2014JoG13J161

Shean, D. E., Head III, J. W., & Marchant, D. R. (2007). Shallow seismic surveys and ice thickness estimates of the Mullins Valley debris-covered glacier, McMurdo Dry Valleys, Antarctica. *Antarctic Science*, *19*(4), 485–496. doi: 10.1017/S0954102007000624

Speirs, J. C., Steinhoff, D. F., McGowan, H. A., Bromwich, D. H., & Monaghan, A. J. (2010). Foehn winds in the McMurdo Dry Valleys, Antarctica: the origin of extreme warming events. *Journal of Climate*, *23*(13), 3577–3598. doi: 10.1175/2010JCLI3382.1

Stein, S., & Wysession, M. (2003). *An Introduction to Seismology, Earthquakes, and Earth Structure.* Malden, MA, USA: Blackwell Publishing.

Wiechecki-Vergara, S., Gray, H. L., & Woodward, W. A. (2001). *Statistical Development in Support of CTBT Monitoring.* Dallas, TX, USA: Southern Methodist University.

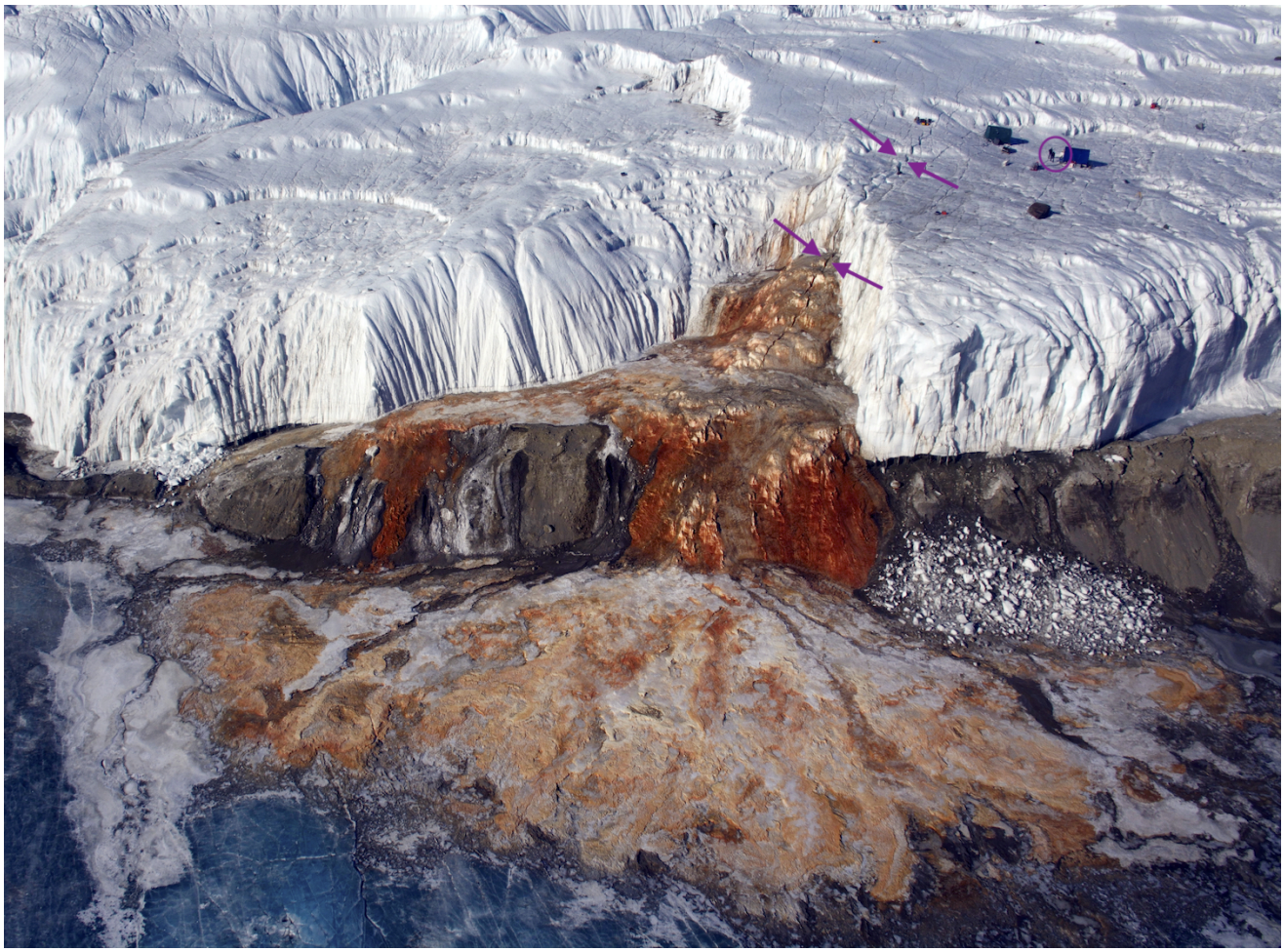

Figure S1. Taylor Glacier terminus following the winter 2014 brine release event. Two sets of purple arrows mark the Blood Falls crevasse; for scale, two people are circled in purple standing next to tents on the glacier surface. Photo: Peter Rejcek, photo date: 21 November 2014. Photo source: National Science Foundation US Antarctic Program Photo Library (https://photolibrary.usap.gov).

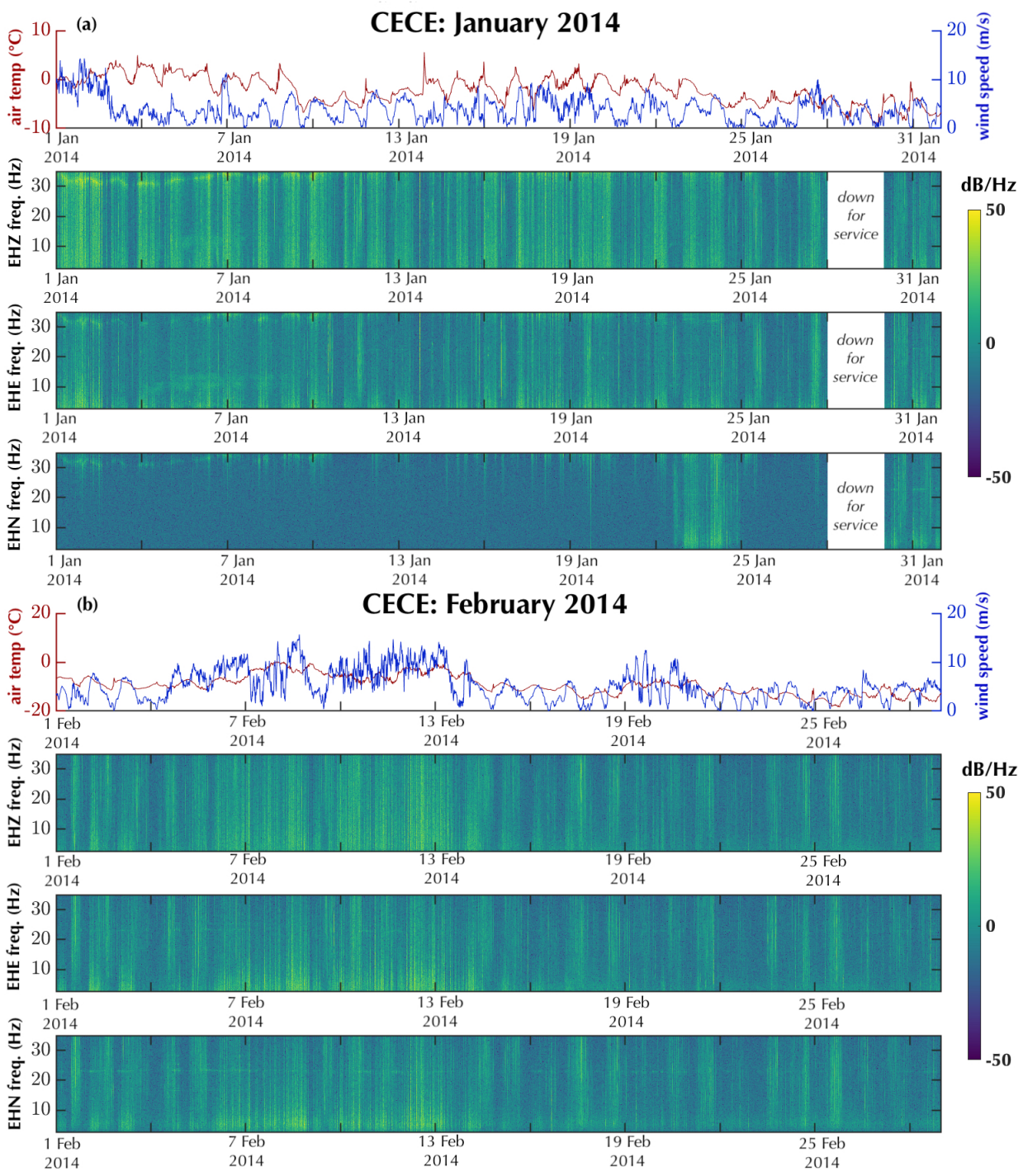

Figure S2. Spectrograms for station CECE for (a) January 2014 and (b) February 2014. Prior to instrument servicing 29 Jan 2014, the north channel (EHN) was not operating properly; the issue was corrected during servicing.

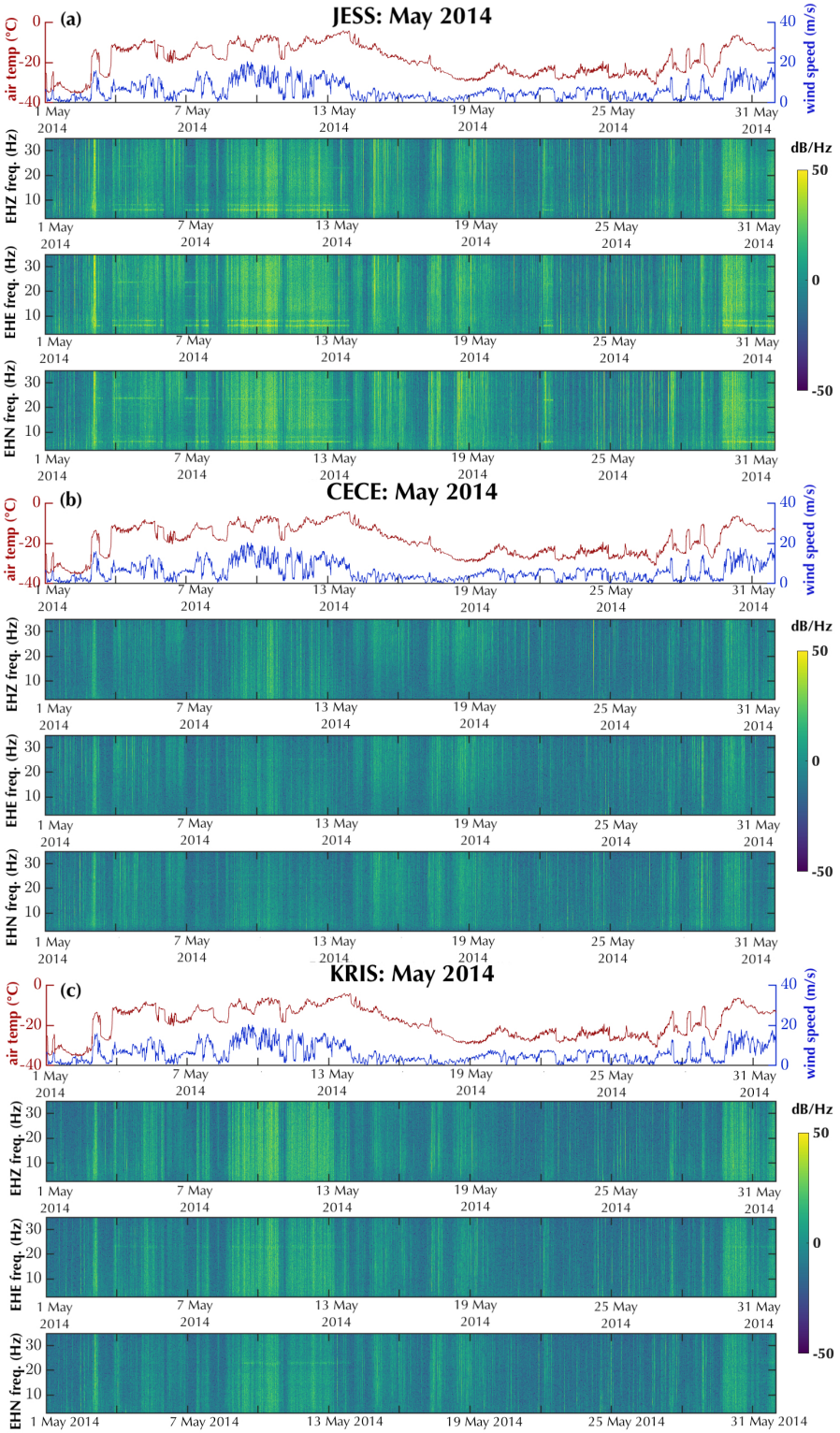

Figure S3. Spectrograms for all stations for May 2014: (a) JESS, (b) CECE, and (c) KRIS.

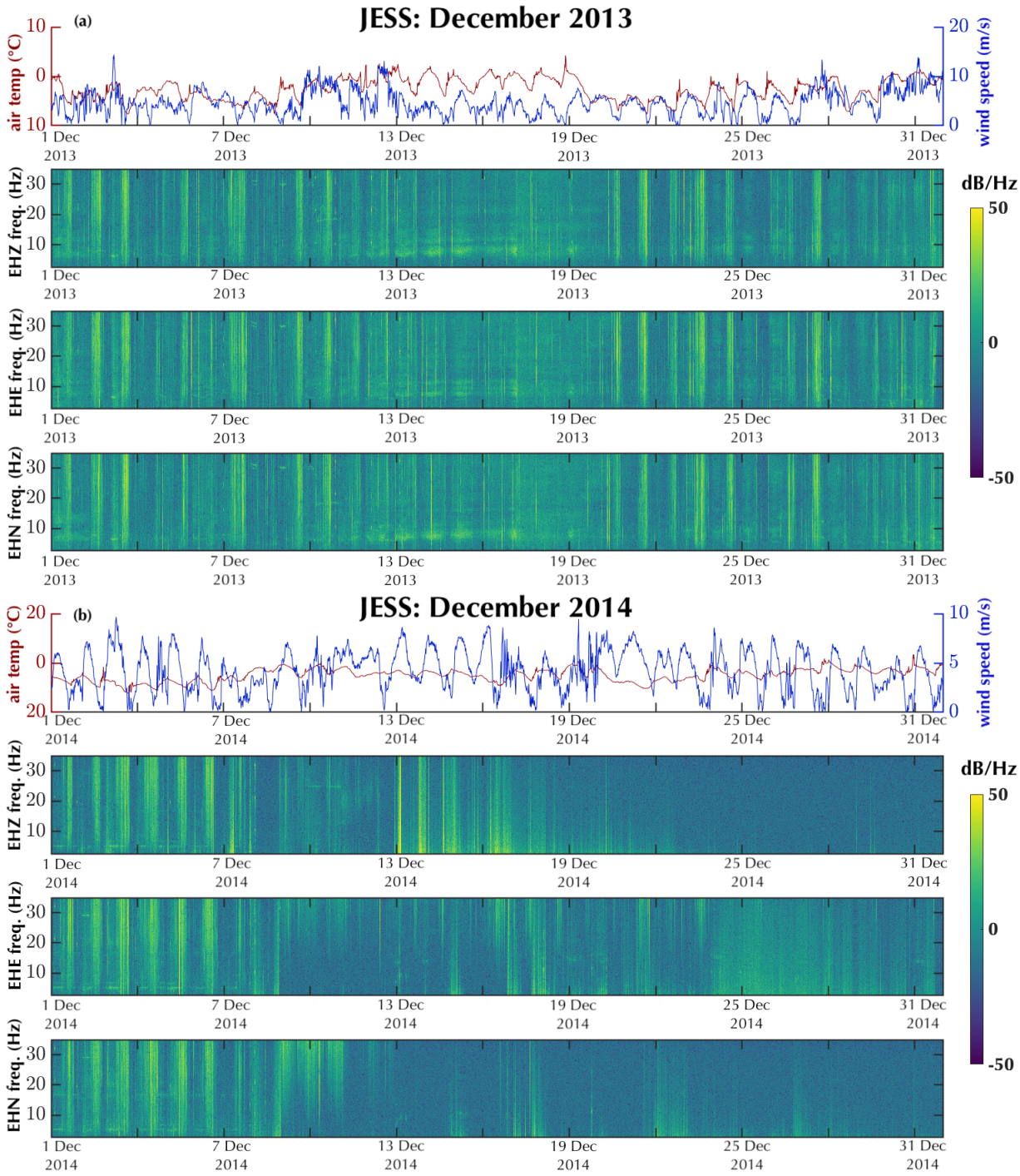

Figure S4. Spectrograms for station JESS for (a) December 2013 and (b) December 2014. During the second week of December 2014, data quality rapidly declines and never improves. Note different scales for temperature and wind speed for the two subplots.

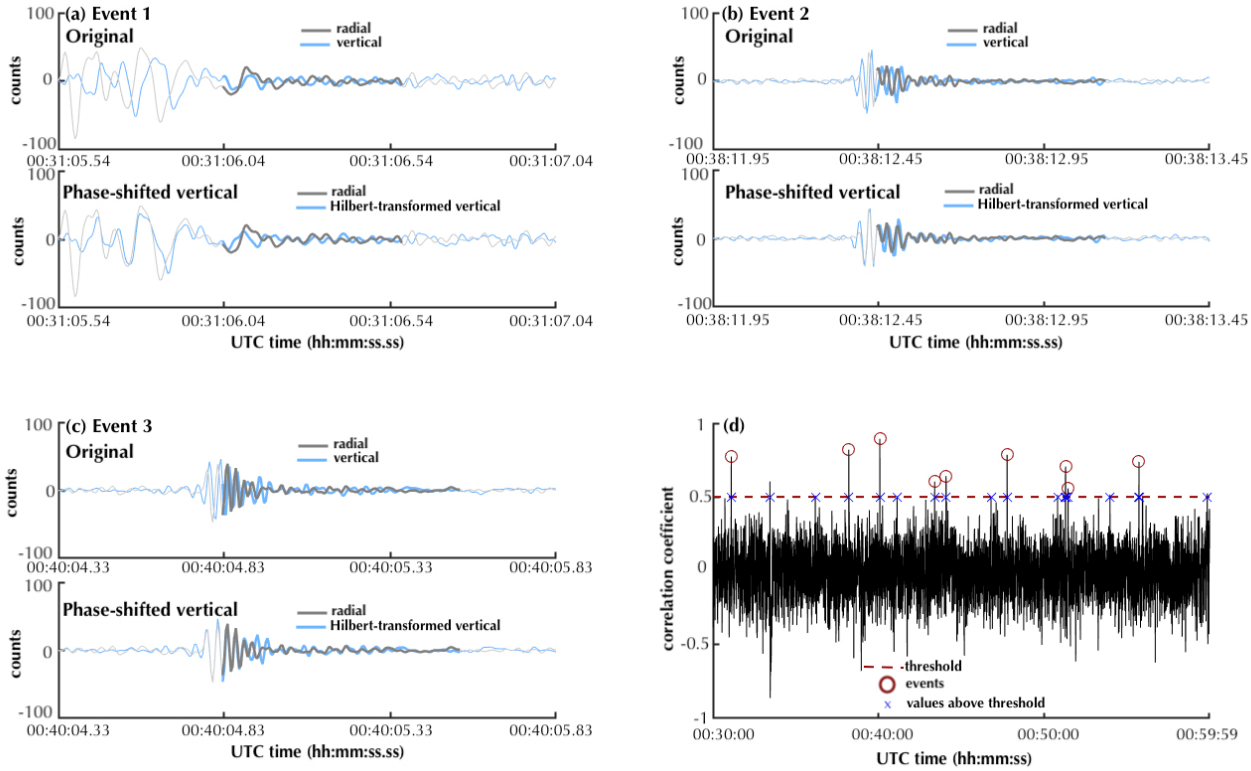

Figure S5. Example waveforms from station CECE on 20 March 2014. In (a)–(c), the upper plot shows the original radial and vertical channels, and the lower plot shows the original radial and phase-shifted vertical channel. The portions of the waveform that triggered the detector are bolded. Event numbers 1-3 correspond to the first three circles in (d). In (d) the Rayleigh wave detector correlation coefficient is plotted for the full 30-minute window. Note different horizontal axes: (a)–(c) span 1.5 seconds, while (d) spans 30 minutes.

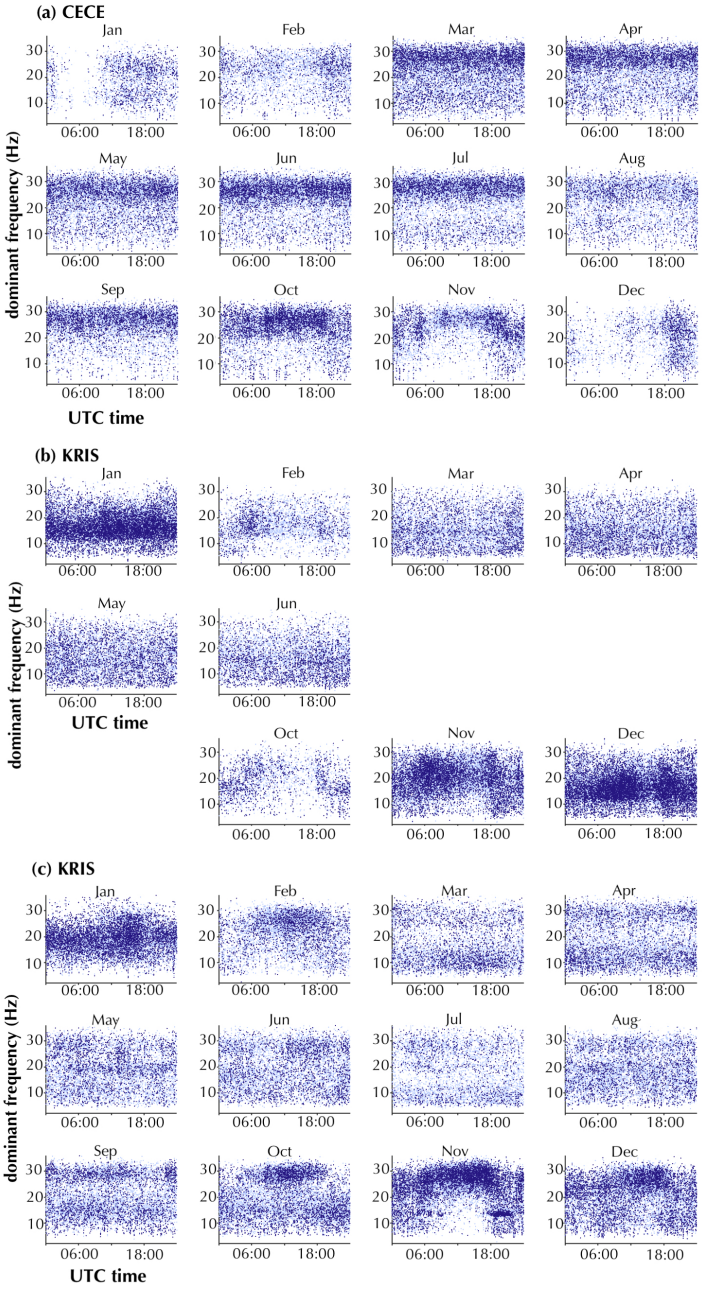

Figure S6. Dominant frequencies of vertical channel data recorded on each station during Rayleigh events (vertical axis, all subplots) and plotted against event time of day (time of day in UTC for all subplots), for a back azimuth oriented towards Blood Falls. Darker data points represent the smaller CFAR value (larger threshold values). Plots for some station/month pairs include data from multiple years. Note all plots have the same axes scales, but some labels are suppressed for readability.

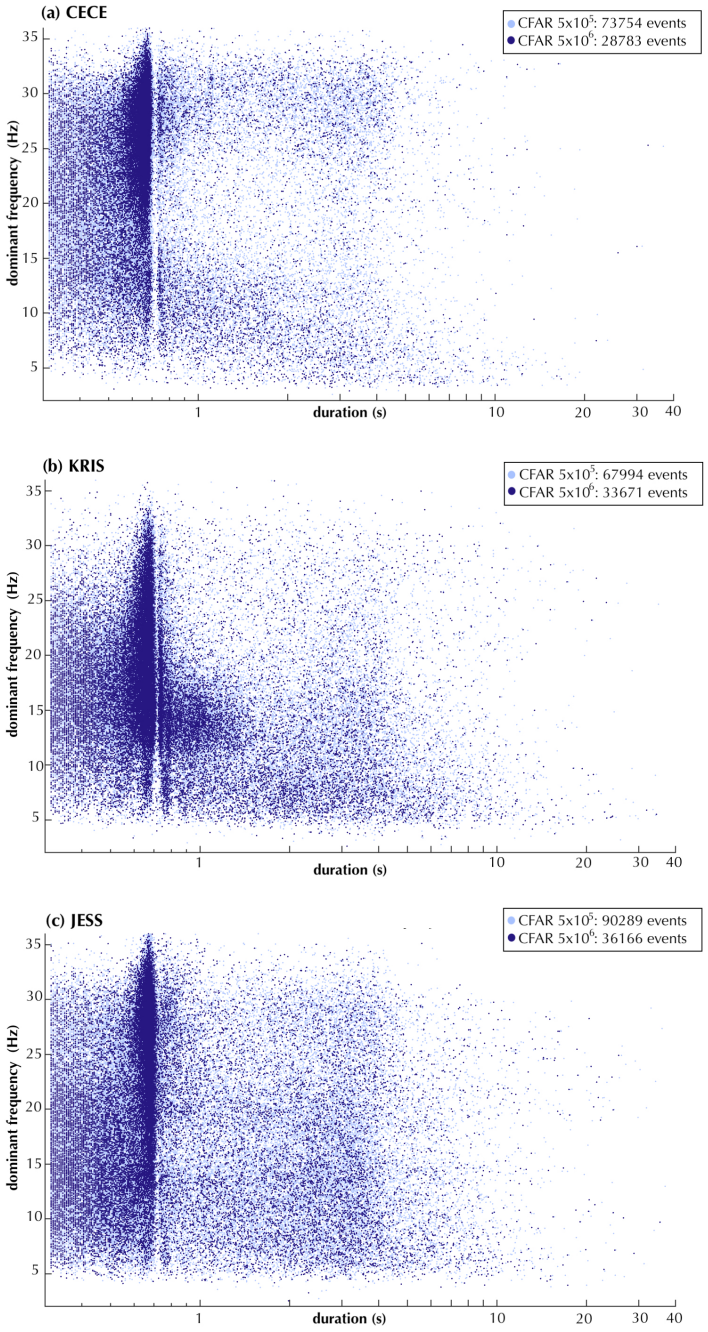

Figure S7. Dominant frequency on the vertical channel and event duration (log scale) for Rayleigh events identified with a Blood Falls back azimuth from each station. Darker colors indicate the smaller CFAR value (higher threshold values). The legend for each plot lists the number of events identified under each CFAR condition, summed over the entire data period.

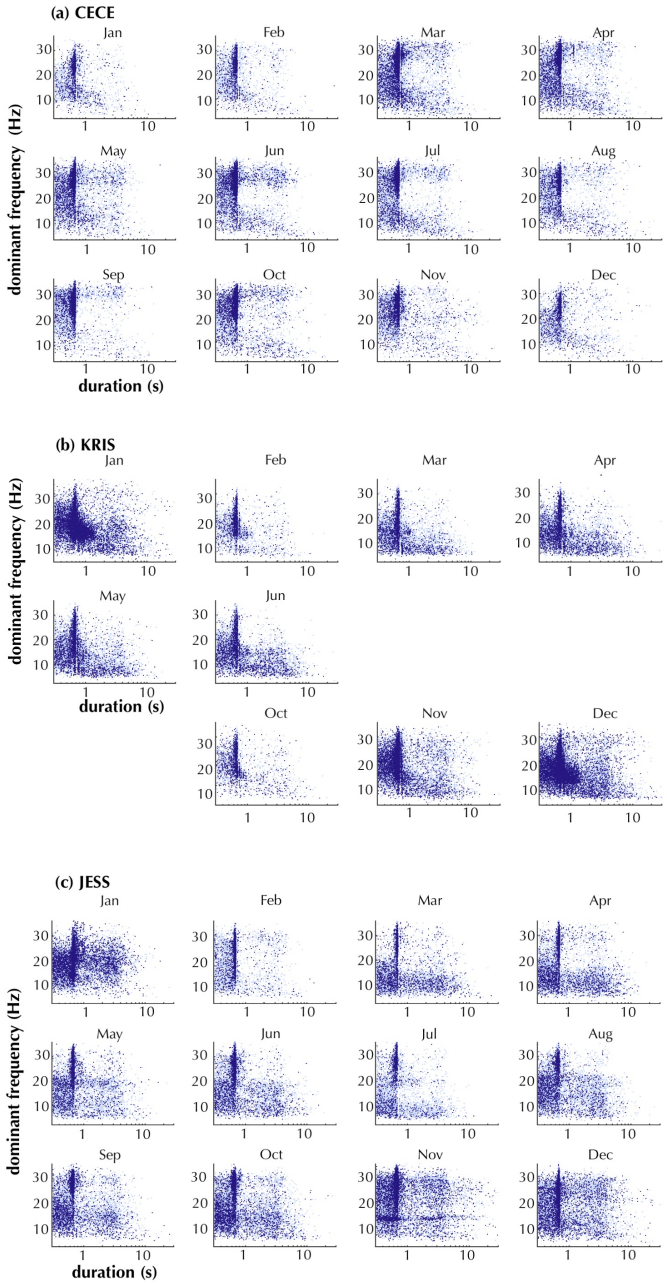

Figure S8. Dominant frequency on the vertical channel during Rayleigh events (vertical axis, all subplots) and event duration (horizontal axis, all subplots) for Blood Falls back azimuth events for each station. Event duration is plotted on a log scale. Darker data points represent the smaller CFAR value (larger threshold values). Plots for some station/month pairs include data from multiple years. Note all plots have the same axes scales, but some labels are suppressed for readability.

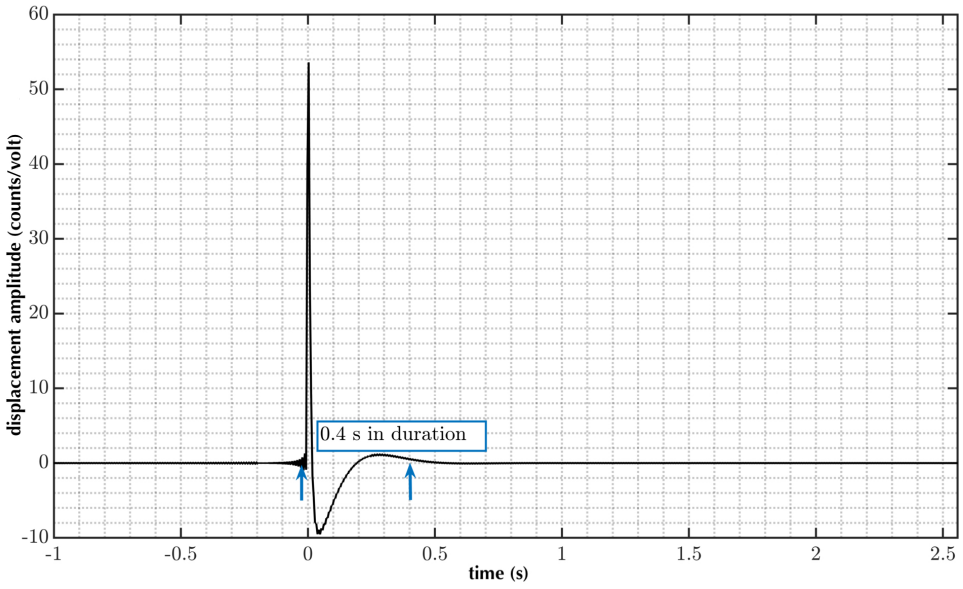

Figure S9. Pulse as observed by a receiver 500 m from the source. To form this pulse, we propagated a delta-function signal from the source to the receiver, with a Futterman filter (Futterman, 1962). We used the following values for the filter parameter $t* = D/Qc_R$: distance ($D = 500\,\mathrm{m}$), quality factor ($Q = 40$), and Rayleigh wave speed ($c_R = 1.7\,\mathrm{km/s}$). This operation dispersively attenuates the source pulse and thereby causally (or nearly so) broadens the pulse. We then convolved this pulse with the L-22 geophone instrument response, which further broadens the pulse. In the absence of noise, such a pulse shows an apparent temporal width of about 0.4 s (blue arrows). The presence of noise would reduce this effective pulse width to be confined to the region that proceeds the large positive swing and includes the broader negative swing back to positive displacement (perhaps 0.2 s). The counts values on the vertical axis are arbitrary in the absence of noise.

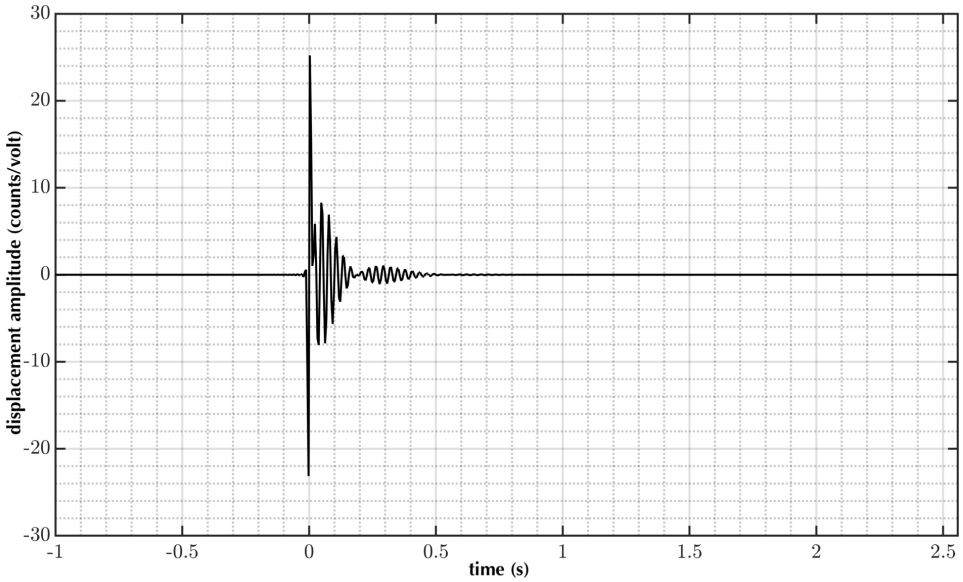

Figure S10. Same as Figure S9, but with a 35Hz source time function superimposed onto the pulse. While the y-scale differs from Figure S9, the counts values on the vertical axis are arbitrary in the absence of noise.

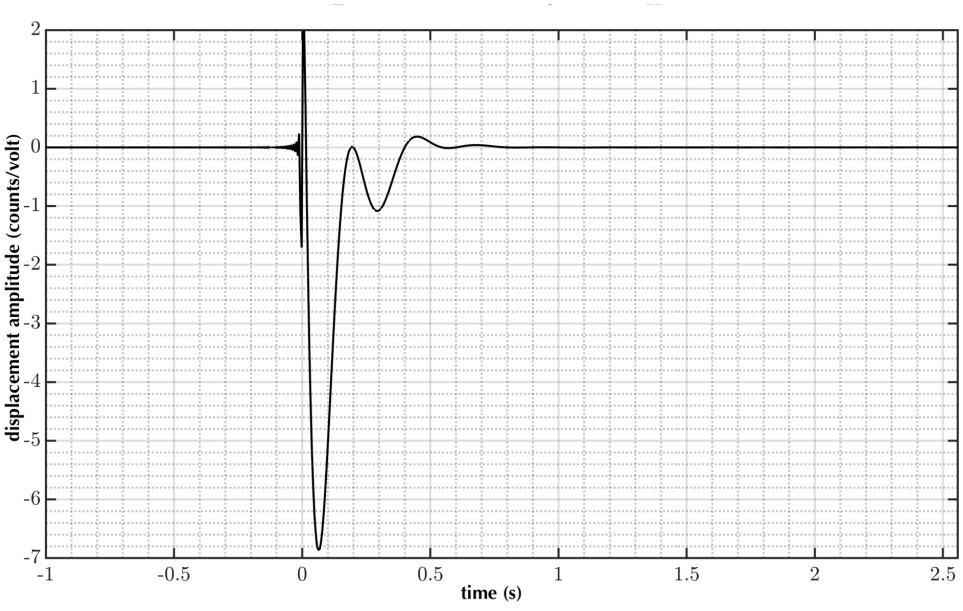

Figure S11. Same as Figure S9, but with a 2.5 Hz source time function superimposed onto the pulse. While the y-scale differs from Figure S9, the counts values on the vertical axis are arbitrary in the absence of noise.

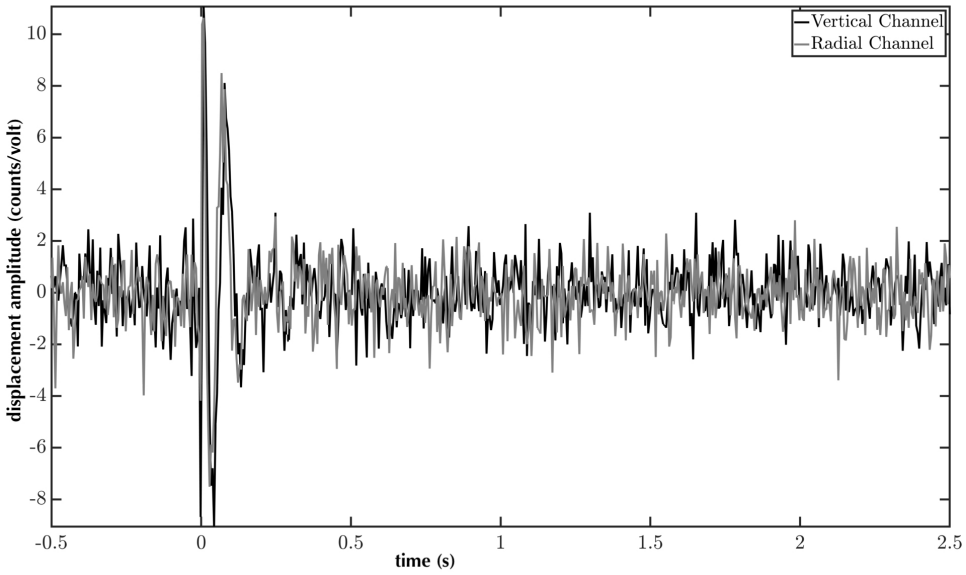

Figure S12. A vertical channel seismogram, phase advanced by 135°(black) compared against a radial channel seismogram (grey).

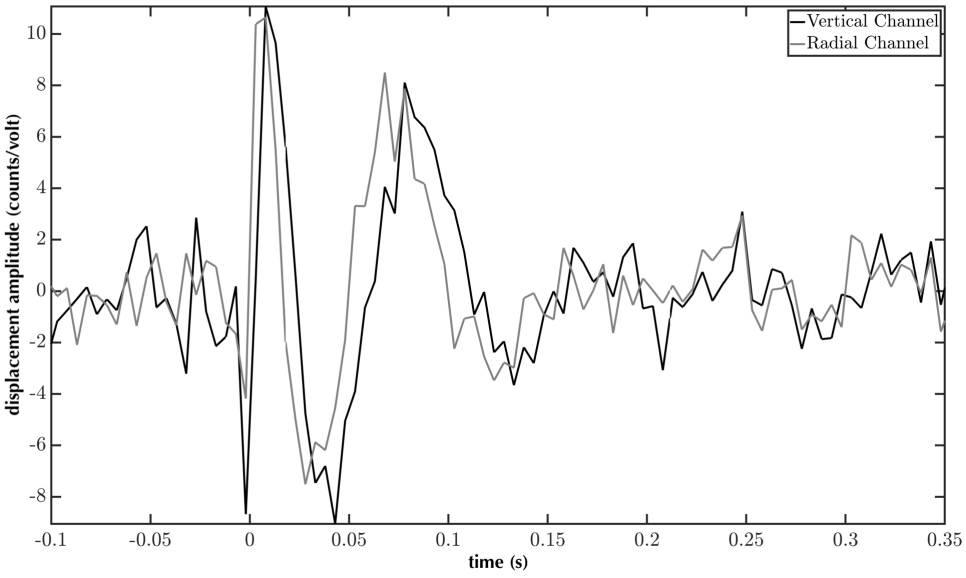

Figure S13. Same as Figure S12, but zoomed in between -0.1 s and 0.35 s to illustrate the visible phase difference.

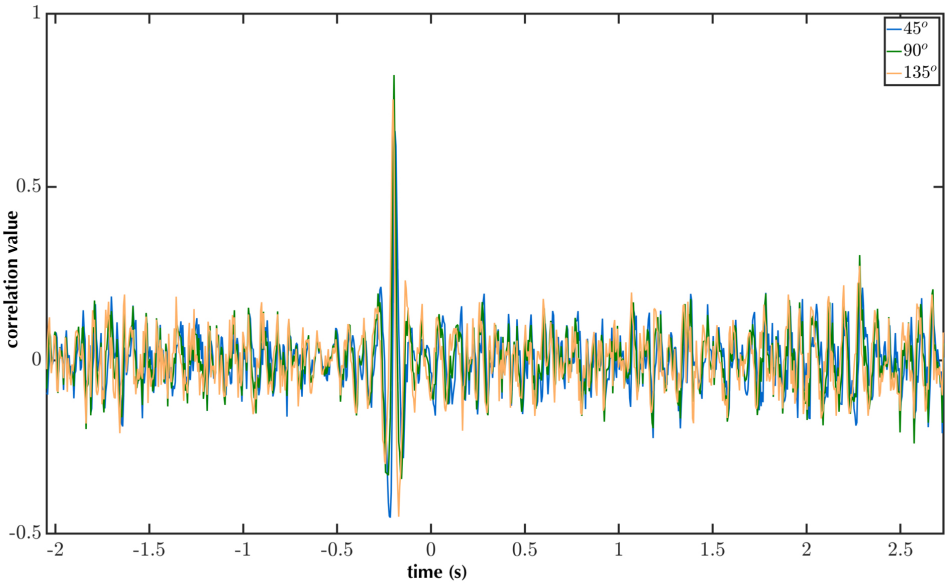

Figure S14. Sample correlation coefficient time series that show the output of a Rayleigh wave detector when the vertical channel seismogram is phase shifted relative to the radial seismogram (phase shifts shown in legend). The vertical axis shows the sample correlation coefficient and is bounded between -1 and 1.

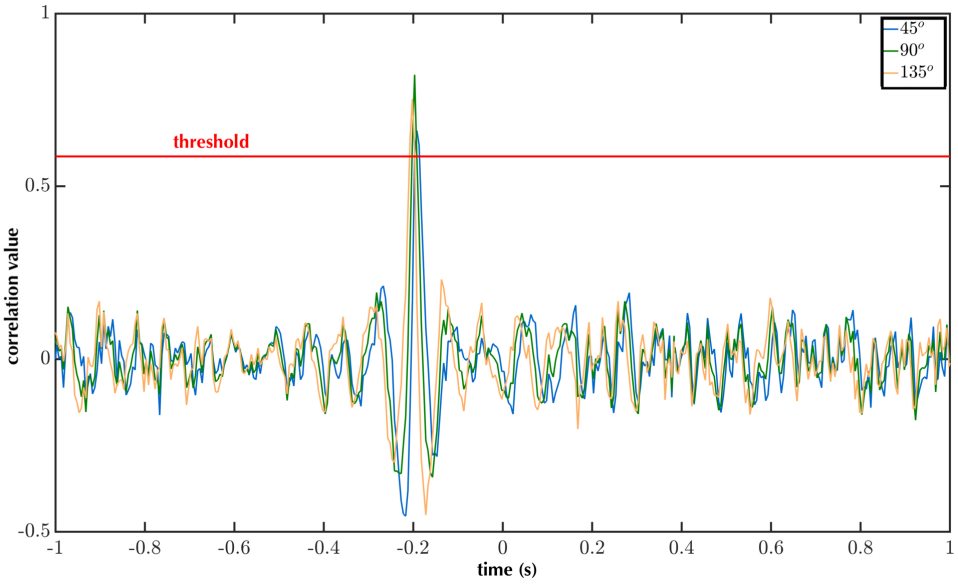

Figure S15. Same as Figure S14, but zoomed in over time -1 to 1 and shown with a threshold for detection that is consistent with the false alarm constraint. The vertical axis shows the sample correlation coefficient and is bounded between -1 and 1, as in Figure S14.

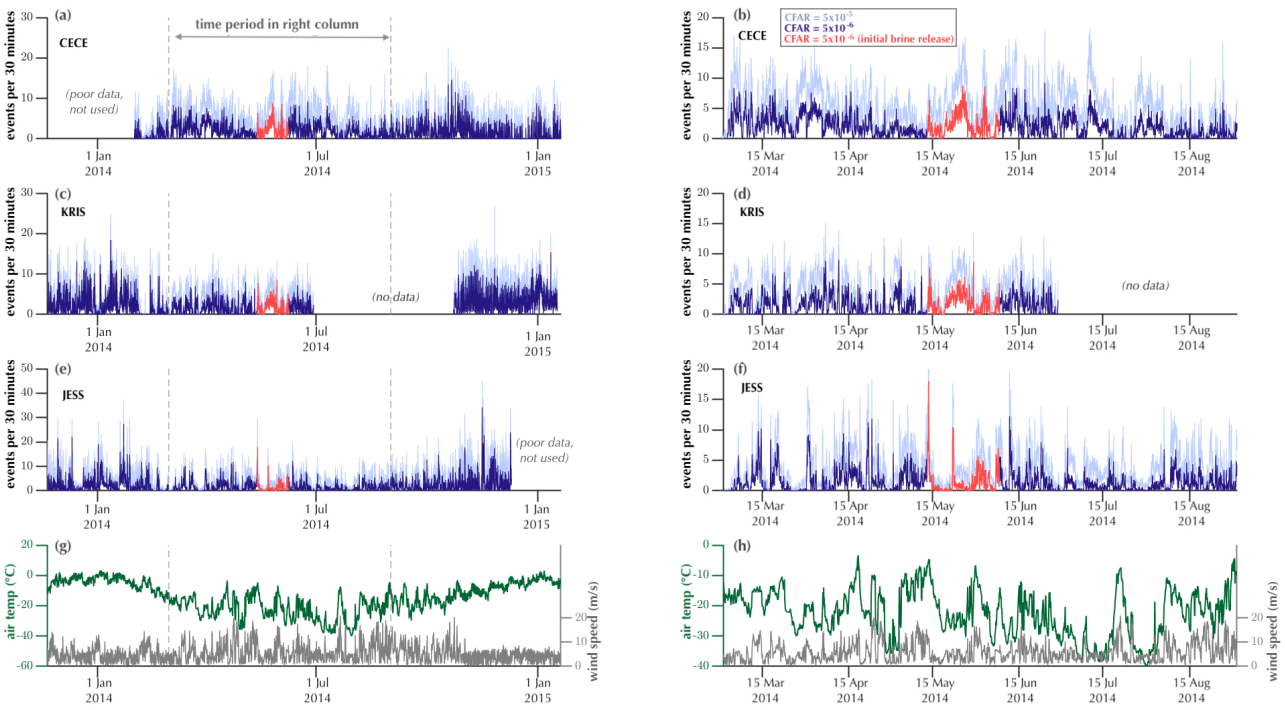

Figure S16. Events per 30 minutes, as identified by the Rayleigh-wave detector at (a, b) land-based station CECE, (c, d) land-based station KRIS (power failure caused data loss after June 30), and (e, f) on-ice station JESS (for this station, in the detail panel (d) only, some rates above 20 events per 30 minutes identified using the $5x10^{-5}$ CFAR are cut off by the vertical scale). Note different vertical scales on panels (a), (c), and (e). The CFAR = $5x10^{-6}$ condition is highlighted in dark blue and red (red indicates initial visible brine release period 13 May – 8 June 2014), and the $5x10^{-5}$ CFAR condition results are in light blue to show the range in detected event rates. In (g, h), air temperature (green, left vertical axis) and wind speed (gray, right vertical axis) from the nearby Taylor Glacier meteorological station (Doran & Fountain, 2019) are plotted. All time series are smoothed with a 2-hour duration (event detection rates: 5-point, weather data: 9-point) moving window.

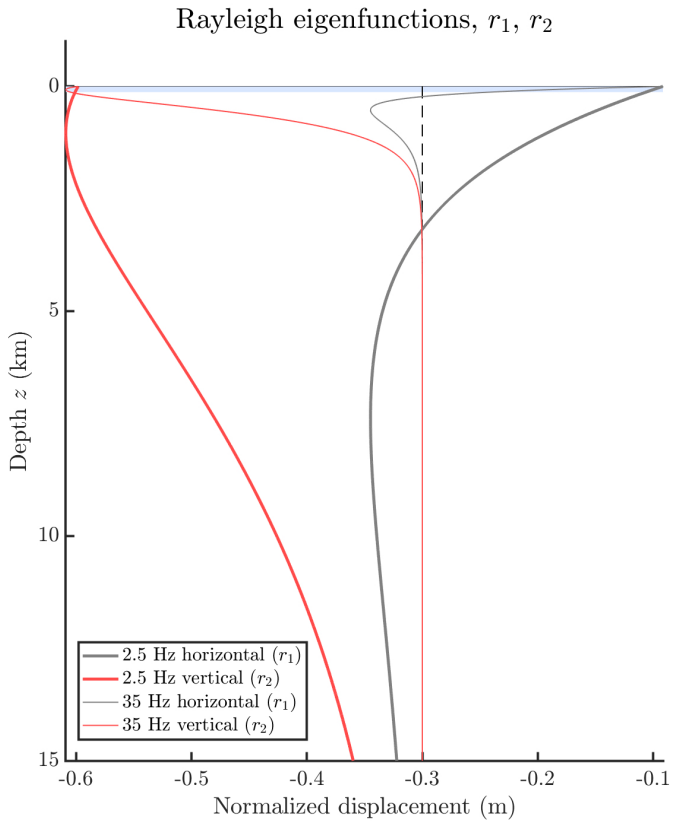

Figure S17. Frequency-dependent, normalized vertical and horizontal displacement as a function of depth, calculated for the eigenfunctions described in the text. The light blue layer represents the 50 m-thick glacier in our model.

Figure S18. Various cracks in ice near the glacier terminus. Cracks include crevasses on the glacier near the cliff face, cracks in the ice-cored terminal moraine (sediment at left of photo), and in the lake ice where the person is standing. Photo: Chris Carr, photo date: November 2013.

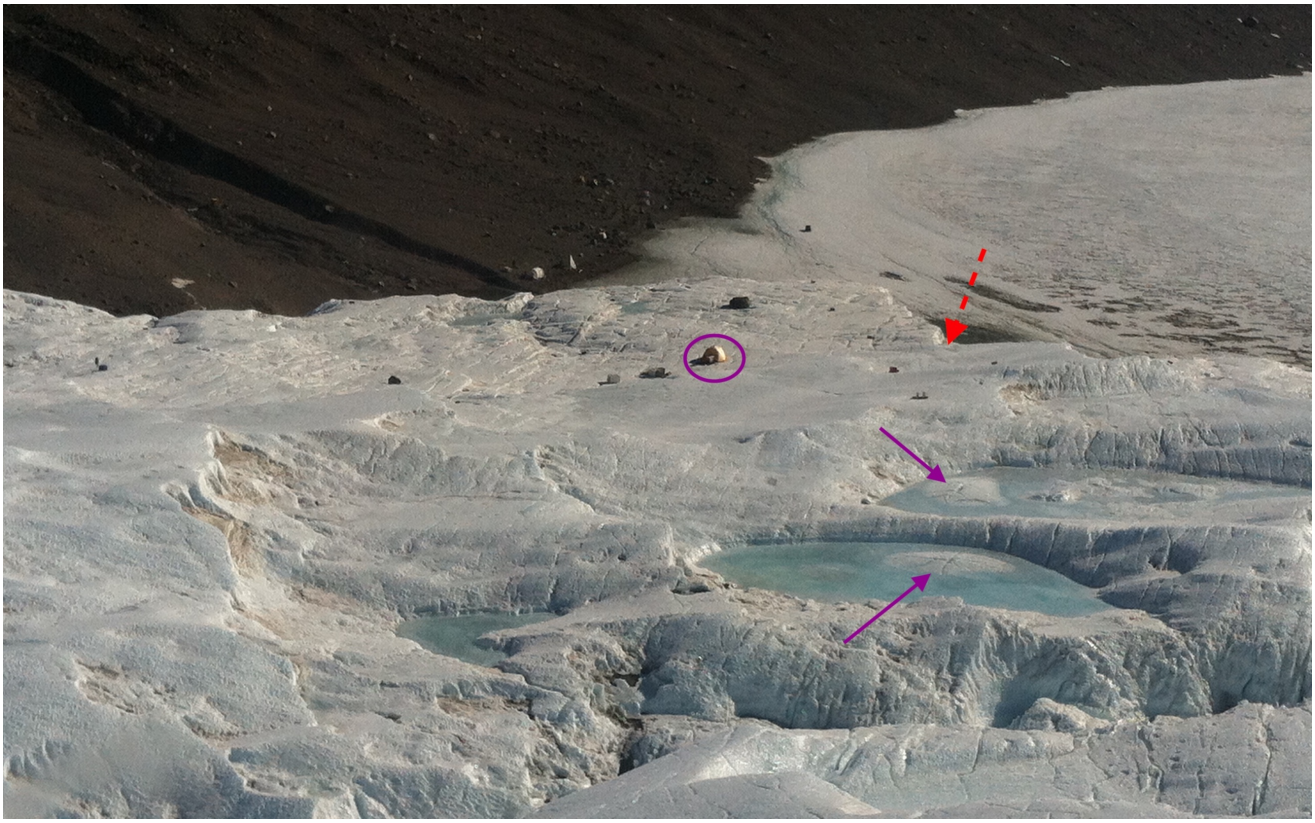

Figure S19. Ice blisters near Blood Falls. Two purple arrows mark ice blisters. The red dashed arrow points to the Blood Falls area of the terminus (out of view). For scale, a tent is circled in purple, this tent is in approximately the same location as the circled people in Figure S1. Photo: Chris Carr, photo date: 11 December 2013.

Table S1. Rayleigh detector threshold values (ρ) and sample variance ($\hat{\sigma}$) for 10–30 May 2014 under the 5x10^{-6} CFAR condition, for a radial direction with the Blood Falls back azimuth. By definition, each 30-minute window has a single threshold value. We estimate the 30-minute window sample variance as the mean of the sample variance of the 15 noise samples from that window. For each noise sample, we calculate the median of the individual sample variances, see table footnotes.

Station	Mean* ρ	Mean** $\hat{\sigma}_R^2$	Mean** $\hat{\sigma}_Z^2$
CECE	0.7049	42.98	59.00
KRIS	0.7248	123.0	658.2
JESS	0.7233	2203	1073

* $\frac{1}{m}\sum_1^m \rho_m$; where $m = 1800$, the number of 30-minute windows.
** $\frac{1}{m}\frac{1}{n}\sum_1^m\sum_1^n[\text{median}(\hat{S}^2)]_{m,n}$; m as above;
and $n = 15$, the number of noise samples.